A study on the energy transfer of a square prism under fluid-elastic galloping

H.G.K.G. Jayatunga, B.T. Tan, J. S. Leontini

Abstract

Extracting useful energy from flow induced vibrations has become a developing area of research in recent years. In this paper, we analyse power transfer of an elastically mounted body under the influence of fluid-elastic galloping. The system and the power transfer is analysed by numerically integrating the quasi-steady state model equations and direct numerical simulations. The power transfer is analysed for both high ($Re = 22300$) and low ($Re = 200$) Reynolds numbers cases.

The linear analysis of the model equation shows that the system is governed by two parameters, namely the combined mass-stiffness parameter Π_1 and the combined mass damping parameter Π_2. A combined mass-damping coefficient, Π_2, that can be derived from the equation of motion, is shown to be the parameter that governs power output. The system is a balance between the power delivered to the system due to fluid-dynamic forcing and power removed through mechanical damping which are governed by the fluid-dynamic forcing characteristics (i.e. the lift force as a function of incident angle) and mechanical damping coefficient as represented by Π_2 respectively. Comparing the DNS results with the QSS data uncovered that a good agreement of the data could be obtained even at low Reynolds numbers when the mass-stiffness,Π_1, is high representing a high mass to stiffness ratio. At low Π_1, the system shows a significant response to forces associated with shedding and this is shown to suppress the galloping response.

Keywords:

1. Introduction

Fluid-elastic galloping is one of the sub-areas of research in fluid structure interactions. This area has been of interest due to the vibrations crated by galloping on transmission lines (Parkinson and Smith (1964)) and civil structures and leading them to failure. Therefore understanding this phenomenon in order to suppresses these vibrations was quite important. However, the search for alternate energy sources with minimal environmental impact has become an important area of research in the modern word. Therefore researchers are moving towards investigating the possibility of extracting useful energy from this vibrations rather than suppressing them Barrero-Gil et al. (2010). Thus, it is quite important to understand the governing parameters and analyse the influence of them on the energy transfer from the fluid to the structure, because this understanding will lead to develop better practical applications. Hence, in this paper the energy transfer from the fluid to the body and isolate the governing parameters influencing it.

According to Païdoussis et al. (2010), Glauert (1919) provided a criterion for galloping by considering the auto-rotation of an aerofoil. Den Hartog (1956) provided a theoretical explanation for galloping for iced electric transmission lines. A weakly non-linear theoretical aeroelastic model to predict the response of galloping was developed by Parkinson and Smith (1964) based on the quasi-steady state hypothesis. Experimental lift and drag data on a fixed square prism at different angles of attack were used as an input for the theoretical model. It essentially used a curve fit of the transverse force to predict the galloping response. The study managed to achieve a good agreement with experimental data.

However, the QSS model equation when solved analytically assuming a the sinusoidal solution, cannot predict the response for cases with low mass ratios. Joly et al. (2012) observed that finite element simulations show a sudden change in amplitude below a critical value of the mass ratio. The quasi-oscillator equation in Parkinson and Smith (1964) was altered to account for the vortex shedding and solved numerically to predict the reduced displacement amplitude at low mass ratios to the point where galloping is no longer present. Barrero-Gil et al. (2010) investigated the possibility of extracting power from vibrations caused by galloping using the quasi-steady state model. So far the studies on galloping using quasi-steady state assumption has been mainly focused on understanding the behaviour of the displacement amplitude Parkinson and Smith (1964), Joly et al. (2012) and Luo et al. (2003) are some examples. However, it is quite important to analyse the behaviour of the velocity when studying the power transfer from the fluid to the body. This is because instantaneous power from the fluid flow to the system is the product of the fluid dynamic force and the velocity of the system while instantaneous power out of the systm is the product of the damping and the velocity of the system. The fluid dynamic force is also modelled to be only dependent on the velocity of the system. This study also focuses on how well the QSS model perform at high damping at low Reynolds numbers.

Here, the modified QSS model is integrated numerically for low Reynolds numbers. The power transfer from the fluid to the structure and the influence of mechanical parameters was investigated (i.e. mass, stiffness and damping). To this end, a series of previously mentioned mechanical parameters are tested at two different values of Re: $Re = 200$, a case that should remain laminar and closer to two-dimensional behaviour; $Re = 22300$, a case where the flow is expected to be turbulent and three-dimensional. Both cases require the input of transverse force coefficients C_y as a function of angle of attack θ for a fixed body. These data are provided from direct numerical simulations for the $Re = 200$ case, while the data provided by Parkinson and Smith (1964) are used for the $Re = 22300$ case.

The structure of the paper is as follows. Section 2 presents the governing equations and the oscillator model used to obtain data and introduces the method for the calculation of the power transferred from the fluid to the structure. Section 3 introduces the governing parameters namely, the combined mass-stiffness Π_1 and the combined mass-damping Π_2, obtained using linearised time scales of the oscillator model. The fixed body tests at a range of θ followed by the response characteristics predicted by the integration of the QSS model for both the high and low Re cases. For the low Re case, the results of the QSS model are compared to those of direct numerical simulations of the fluid-structure interaction problem. Finally, section 4 presents the conclusions that can be drawn from this work.

Nomenclature

a_1, a_3, a_5, a_7	coefficients of the polynomial to determine C_y
A	displacement amplitude
c	damping constant
D	characteristic length (side length) of the cross section of the body
$f = \sqrt{k/m}/2\pi$	natural frequency of the system
F_y	instantaneous force normal to the flow
F_0	amplitude of the oscillatory force due to vortex shedding
k	spring constant
m	mass of the body
m_a	added mass
P_d	power dissipated due to mechanical damping
$P_{in} = \rho U^3 D/2$	Energy flux of the approaching flow
P_{mean}	mean power
P_t	power transferred to the body by the fluid
t	time
U	freestream velocity
U_i	Induced velocity
$y, \dot{y}, \ddot{y}$	transverse displacement, velocity and acceleration of the body
$\mathcal{A} = DL$	frontal area of the body
λ	Inverse time scale of a galloping dominated flow
$\lambda_{1,2}$	Eigenvalues of linearized equation of motion
ρ	fluid density
$\omega_n = 2\pi f$	natural angular frequency of the system
ω_s	vortex shedding angular frequency
$c^* = cD/mU$	non-dimensionalised damping factor
$C_y = F_y/0.5\rho U^2 DL$	normal (lift) force coefficient
$m^* = m/\rho D^2 L$	mass ratio
Re	Reynolds number
$U^* = U/fD$	reduced velocity
$Y = y/D$	non-dimensional transverse displacement
$\dot{Y} = m^* \dot{y}/a_1 U$	non-dimensional transverse velocity
$\ddot{Y} = m^{*2} D\ddot{y}/a_1^2 U^2$	non-dimensional transverse acceleration
$\Gamma_1 = 4\pi^2 m^{*2}/U^{*2} a_1^2$	First dimensionless group arising from linearised, non-dimensionalise
$\Gamma_2 = c^* m^*/a_1$	Second dimensionless group arising from linearised, non-dimensional
$\zeta = c/2m\omega_n$	damping ratio
$\theta = \tan^{-1}(\dot{y}/U)$	instantaneous angle of incidence (angle of attack)
$\Pi_1 = 4\pi^2 m^{*2}/U^{*2}$	Combined mass-stiffness parameter
$\Pi_2 = c^* m^*$	Combined mass-damping parameter

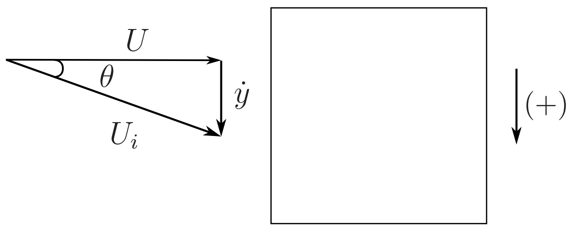

Figure 1: Induced angle of attack on the square prism due to the resultant of free-stream velocity of the fluid and transverse velocity of the body.

2. Problem formulation and methodology

2.1. The quasi-steady state (QSS) model

The equation of motion of the body is given by

$$(m)\ddot{y} + c\dot{y} + ky = F_y, \tag{1}$$

where the forcing term F_y is given by

$$F_y = \frac{1}{2}\rho U^2 \mathcal{A} C_y. \tag{2}$$

In the QSS model, it is assumed that the force on the body at a given instantaneous incident angle θ (defined in figure 1) is the same as the mean force on a static body at the same incident angle, or angle of attack. The instantaneous value of C_y is therefore determined by an interpolating polynomial based on the lift data for flow over a stationary body at various θ. Using the relationship between θ and the instantaneous transverse velocity of the body $\dot{y}$ shown in figure 1, C_y can be written as a function of $\dot{y}$. The order of the interpolation polynomial used to define this function has varied from study to study. For example a 7^{th} order polynomial was used in Parkinson and Smith (1964) and 3^{rd} order polynomial was used in Barrero-Gil et al. (2009). Ng et al. (2005) concluded that using a 7^{th} order polynomial is sufficient and a polynomial higher than that of 7^{th} order doesn't provides a significantly better result. Thus a 7^{th} order interpolating polynomial is used in this present study. As a result, $C_y(\theta)$ (noting that theta is proportional to $\dot{y}/U$) is defined as

$$C_y(\theta) = a_1\left(\frac{\dot{y}}{U}\right) + a_3\left(\frac{\dot{y}}{U}\right)^3 + a_5\left(\frac{\dot{y}}{U}\right)^5 + a_7\left(\frac{\dot{y}}{U}\right)^7. \tag{3}$$

It is expected that vortex shedding will be well correlated along the span and provide significant forcing at low Re. Joly et al. (2012) introduced an additional sinusoidal forcing function to the hydrodynamic forcing to model this. This enables the model to provide accurate predictions even at low mass ratios where galloping excitation is suppressed or not present. This study intends to identify the parameter space where the QSS model predicts well and therefore the additional sinusoidal forcing function is disregarded. ***KJ: Kenny's openion is that we need to justify this by saying fixed amplitude and fixed frequency does not accurately predict shedding forces (I need some references for this. Do you have any since you have been doing VIV research for a square cross section). What we have to say that what the sinusoidal function joly used does not apply to a universal case. i.e. No single value can accurately model the shedding forces across a brorad range of parameters with damping. ***

$$m\ddot{y}+c\dot{y}+ky=\frac{1}{2}\rho U^2\mathcal{A}\left(a_1\left(\frac{\dot{y}}{U}\right)+a_3\left(\frac{\dot{y}}{U}\right)^3+a_5\left(\frac{\dot{y}}{U}\right)^5+a_7\left(\frac{\dot{y}}{U}\right)^7\right. \quad (4)$$

This equation can be solved using standard time integration methods. In this study the fourth-order Runge-Kutta scheme built in to the MATLAB routine 'ode45' was generally used to obtain the solutions.

2.2. Calculation of average power

The dissipated power due to the mechanical damping represents the ideal potential amount of harvested power output. Therefore, the mean power output can be given by

$$P_{mean} = \frac{1}{T}\int_0^T (c\dot{y})\dot{y}dt, \quad (5)$$

where T is the period of integration and c is the mechanical damping constant.

It should be noted that this quantity is equal to the work done on the body by the fluid, defined as

$$P_{mean} = \frac{1}{T}\int_0^T F_y\dot{y}dt, \quad (6)$$

where F_y is the transverse (lift) force.

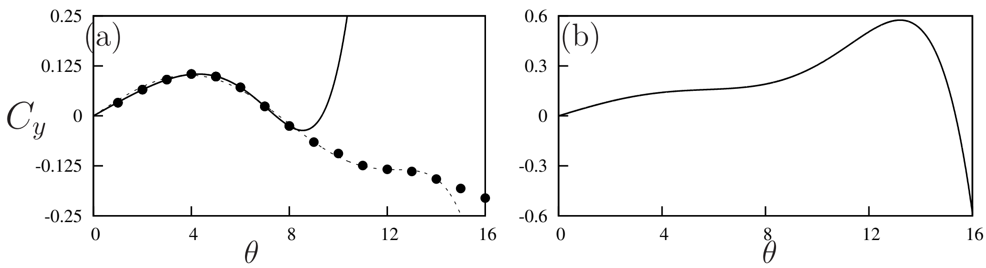

Figure 2: Lift coefficient, C_y, as a function of incidence angle θ, for a static square cross section. (a) Data from simulations at $Re = 200$ (b) data from Parkinson and Smith (1964) at $Re = 22300$. Points (•) are measurements from the simulations. At $Re = 200$ two interpolation polynomials are used where C_y where $\theta \leq 7°$ is represented by (—) and $\theta \leq 7°$ (- - -). All curves in both plots are 7th-order interpolating polynomials used to predict the fluid forcing for the QSS model. C_y is the force coefficient of the force which occurs normal to the induced velocity. ***KJ: Kenny wants to put only one curve what do you think ?. We actually used two curves to get more accuracy ***

have to repharase These two definitions show two important interpretations of the power with respect to any energy production device. The first shows that power is a balance between transverse velocity nd mechanical damping ; with an optimal balance of the two get maximum power output The second shows that power will be high for situations where the transverse force and the body velocity are in phase.

Case	a_1	a_3	a_5	a_7
Re=200 (polynomial-1)	1.97	71.3	-6937	-254943
Re=200 (polynomial-2)	2.32	197.8	4301.7	30311.9
Re=22300	2.69	168	1670	59900

Table 1: Coefficient values used in the 7th order interpolation polynomial for high ($Re = 22300$) and low ($Re = 200$) Reynolds numbers. Polynomial-1 was used to predict the C_y at $\theta \leq 7°$ while polynomial-2 was used to predict the C_y where $\theta > 7^c irc$ in order to obtain a better fit. These data are used as input data to calculate the right-hand side of Eq. 4 throughout this study.

2.3. Parameters used

For the low Re tests, $Re = 200$ was maintained. Stationary C_y data were obtained at different angles of attack ranging from $0°$ to $16°$. The average power was obtained by using equation 5, and the averaging was done over no less than 20 galloping periods. Predictions of power output at $Re = 22300$ were obtained using the coefficients for curve fitting C_y (Table (1)) from Parkinson and Smith (1964), in order to provide a comparison between high and low Reynolds numbers. The mass ratio m^* was kept at 1163 for $Re = 22300$ (Similar to Parkinson and Smith (1964)) and $m^* = 20$ for Re=200. These parameters were used throughout this study unless otherwise specified.

The stationary data and the fluid-structure interaction (FSI) data were obtained using a high-order spectral element routine to simulate the two-dimensional laminar flow. Simulations involving fluid structure interaction (FSI) were used to provide additional validation of the QSS model. The inlet was placed $20D$ while the outlet situated $60D$ away from the centroid of the body. The side boundaries were placed $20D$ away from the centroid of the body where D was kept as unity throughout this study. The Navier–Stokes equations were solved in an accelerated frame of reference attached to the moving body along with the body equation of motion given in equation 1. A three-step time splitting scheme together with high-order Lagrangian polynomials were used to obtain the solution. The details of the method can be found in Thompson et al. (2006, 1996). This code has been very well validated in a variety of fluid-structure interaction problems (Leontini et al., 2007; Griffith et al., 2011; Leontini et al., 2011; Leontini and Thompson, 2013).

The computational domain consists of 751 quadrilateral macro elements where the majority of the elements were concentrated near the square section. A freestream condition was given to the inlet, top and bottom boundaries and the normal velocity gradient was set to zero at the outlet. A convergence study was performed by changing the order of the polynomial (p-refinement) at $U^* = 40$ and $Re = 200$. A 9^{th} order polynomial together with a time step of $\Delta tU/D = 0.001$ was sufficient to ensure an accuracy of 2% with regards to amplitude of oscillation.

3. Results

Figure 2 shows the plots of the interpolation polynomials as a function of θ. For high Re the polynomial incorporated by Parkinson and Smith (1964) was used. For low Re two polynomials were used to obtain a better fit to the data. One to fit data from $\theta = 0^0 \rightarrow 7^0$ and the other $\theta > 7^0$. There are several differences that can be observed between high and low Reynolds number data. The peak value of C_y is significantly lower at $Re = 200$ ($C_y =$ 0.12 at 5°) compared to $Re = 22300$ ($C_y = 0.57$ at 13°) . The inflection point present around 8° for $Re = 22300$ is not present at $Re = 200$. This agrees with the findings of Luo et al. (2003). It was concluded by Luo et al. (2003) that hysteresis in the system response occurs due to the inflection point in the C_y curve. Therefore hysteresis is not expected at $Re = 200$.

The range of incident flow angles where C_y remains positive is narrow at $Re = 200$ ($0° < \theta \leq 7°$) compared to $Re = 22300$ ($0° < \theta \leq 15°$). This feature is what sustains galloping. Power is only transferred from the fluid to the supporting structure within this range of incident angles because fluid forces are acting in the direction of travel of the oscillating body, as demonstrated by equation 6. Incident angles beyond this range actually suppress the galloping and power goes in the opposite direction, i.e; from body to fluid. Therefore due to the overall smaller C_y and narrow range of angles where C_y is positive for $Re = 200$ compared to $Re = 22300$, it is expected that the transferred power at $Re = 200$ is significantly lower than at $Re = 22300$.

The natural time scales of the system can be found by solving for the eigenvalues of the linearised equation of motion, namely

$$(m)\ddot{y}+c\dot{y}+ky=\frac{1}{2}\rho U^2 \mathcal{A} a_1 \left(\frac{\dot{y}}{U}\right), \tag{7}$$

which is a simplified version og the equation of motion presented in equation 4 with the polynomial series for the lift force truncated at the linear term.

Combining the $\dot{y}$ terms and solving for eigenvalues gives

$$\lambda_{1,2} = -\frac{1}{2}\frac{c - \frac{1}{2}\rho U \mathcal{A} a_1}{(m)} \pm \frac{1}{2}\sqrt{\left[\frac{c - \frac{1}{2}\rho U \mathcal{A} a_1}{(m)}\right]^2 - 4\frac{k}{(m+m_a)}}. \tag{8}$$

If it is assumed that the spring is relatively weak, $k \rightarrow 0$, a single non-zero eigenvalue remains. This eigenvalue is

$$\lambda = -\frac{c - \frac{1}{2}\rho U \mathcal{A} a_1}{(m)}. \tag{9}$$

Further, if it is assumed that the mechanical damping is significantly weaker than the aerodynamic forces on the body, $c \to 0$ and

$$\lambda = \frac{\frac{1}{2}\rho U \mathcal{A} a_1}{(m)}. \tag{10}$$

In this form, λ represents the inverse time scale of the motion of the body due to the negative damping effect of the long-time aerodynamic forces. In fact, the terms can be regrouped and λ written as

$$\lambda = \frac{a_1}{m^*}\frac{U}{D} \tag{11}$$

Written this way, the important parameters that dictate this inverse time scale are clear. The rate of change in the aerodynamic force with respect to angle of attack when the body is at the equilibrium position, $\partial C_y/\partial\alpha$, is represented by a_1. The mass ratio is represented by m^*. The inverse advective time scale of the incoming flow is represented by the ratio U/D. Increasing a_1 would mean the force on the body would increase more rapidly with small changes in the angle of attack, θ, or transverse velocity. Equation 11 shows that such a change will increase the inverse time scale, or analogously decrease the response time of the body. Increasing the mass of the body, thereby increasing m^*, has the opposite effect. The inverse time scale is decreased, or as might be expected, a heavier body will take longer to respond.

This timescale can then be used to non-dimensionalize the equation of motion, and to find the relevant dimensionless groups of the problem. If the non-dimensional time, τ, is defined such that $\tau = t(a_1/m^*)(U/D)$, the equation of motion presented in equation 4 can be non-dimensionalized as

$$\ddot{Y} + \frac{m^{*2}}{a_1^2}\frac{kD^2}{mU^2}Y = \left(\frac{1}{2} - \frac{m^*}{a_1}\frac{cD}{mU}\right)\dot{Y} + H.O.T., \tag{12}$$

where $H.O.T.$ represents the higher order terms in $\dot{Y}$. The coefficients can be regrouped into combinations of non-dimensional groups, and rewritten as

$$\ddot{Y} + \frac{4\pi^2 m^{*2}}{U^{*2}a_1^2}Y = \left(\frac{1}{2} - \frac{c^* m^*}{a_1}\right)\dot{Y} + H.O.T, \tag{13}$$

where $c^* = cD/mU$ is a non-dimensional damping parameter.

Equation 13 shows there are four non-dimensional parameters that play a role in setting the response of the system. These are the stiffness (represented by the reduced velocity U^*), the damping c^*, the mass ratio m^*, and the geometry, represented by the rate of change in the aerodynamic force with respect to angle of attack when the body is at the equilibrium position, a_1. The grouping of these parameters into two groups in equation 13 which arise by non-dimensionalising using the natural time scale of the galloping system, suggests there are two groups that dictate the response: $\Gamma_1 = 4\pi^2 m^{*2}/U^{*2}a_1^2$ and $\Gamma_2 = c^* m^*/a_1$. For a given geometry and Reynolds number, Γ_1 can be thought of as a combined mass-stiffness, whereas Γ_2 can be thought of a a combined mass-damping parameter. As it is assumed that during galloping the stiffness plays only a minor role, Γ_2 seems a likely parameter to collapse the data presented in figure **??**. In fact, in the classic paper on galloping from Parkinson and Smith (1964), galloping data from wind tunnel tests is presented in terms of a parameter that can be shown to be the same as Γ_2.

All of the quantities that make up Γ_1 and Γ_2 can, in theory, be known before an experiment is conducted. However, the quantity a_1 is a relatively difficult one to determine, requiring static body experiments or simulations. Here, the geometry is unchanged and results are only being compared at the same Re. Hence, suitable parameters can be formed by multiplying Γ_1 and Γ_2 by a_1^2 and a_1 respectively, to arrive at a mass-stiffness parameter $\Pi_1 = 4\pi^2 m^{*2}/U^{*2}$, and a mass-damping parameter defined as $\Pi_2 = c^* m^*$.

Figure **??** shows the comparison of mean power data at $Re = 200$ presented using different independent variables. Sub-figure (a) and (c) shows the displacement and velocity amplitudes respectively and (e) shows the mean power as a function of the classic VIV parameter, $U^*$for various ζ. (b), (d) and (f) shows the same data as a function of Π_2, for various $\Pi_1$both of which were recently derived. The data presented using the classical VIV parameters follows the same trends as Barrero-Gil et al. (2010). However, the data presented using the linearlized parameter shows an excellent collapse for both velocity amplitude and mean power. Therefore, it could be deduced that the mean power of the system is only dependent on Π_2 and not on Π_1. This implies that the natural frequency of the system which is used to scale U^*, ζ and $\Pi_1$does not influence the system in these cases.

Figure 3 have to write something about the optimum power

Hysteresis could be observed for the case with a higher Reynolds number. Different solutions could be obtained by manipulating the initial conditions

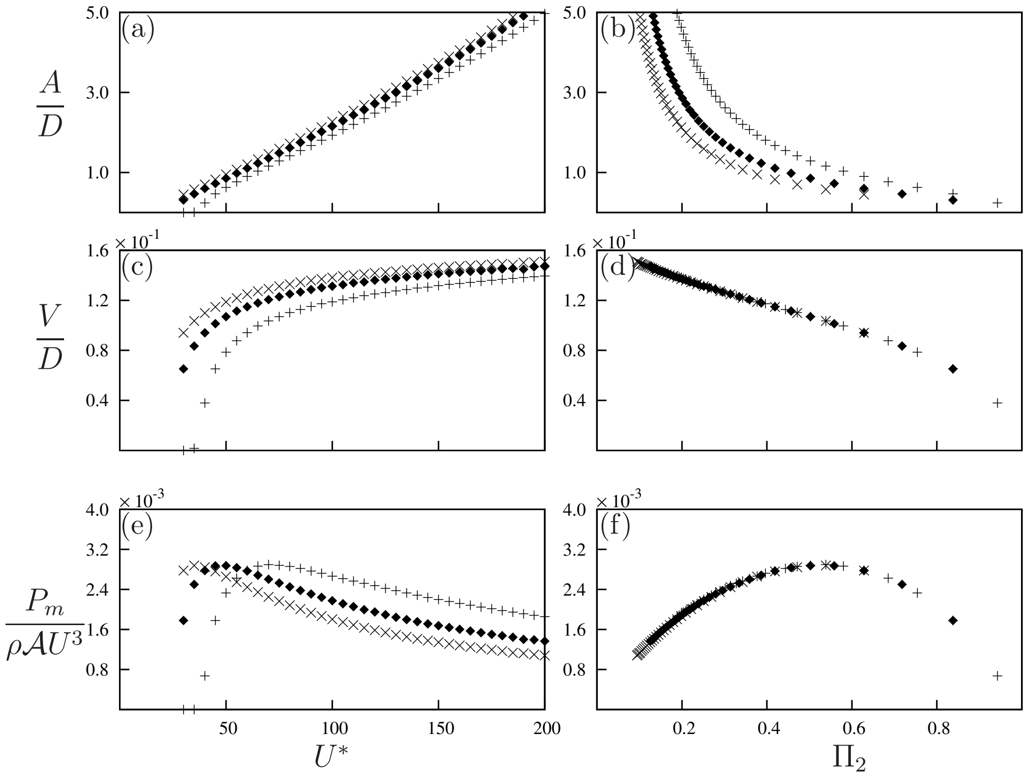

Figure 3: Displacement amplitude, velocity amplitude and mean power data as functions of two different independent varibles. Data presented in (a), (c) and (e) using the classical VIV parameter U^*, obtained at $Re = 200$ and $m^* = 20$ at three different damping ratios: $\zeta = 0.075$ ($\times$), $\zeta = 0.1$ ($\blacklozenge$) and $\zeta = 0.15$ ($+$). (b) (d) and (f) are the same data presented using the combined mass-damping parameter (Π_2) as the independent variable.

(initial displacement) of the system. The upper branch was obtained by giving an initial displacement which was higher than the expected amplitude while the lower branch was obtained by providing a lower initial displacement than the expected amplitude. Although theory shows a possible third state, it is an unstable branch and as such it could not be achieved numerically. This was also observed by Vio et al. (2007).

3.1. Displacement, velocity and power

The instantaneous power from the fluid to the body can be expressed as $P_t = F_y\dot{y}$. Similarly the dissipated power due to the mechanical damping can be expressed as $P_d = (c\dot{y})\dot{y}$. The time average of these two quantities, described in equations 5 and 6 should be equal due to energy conservation, provided that the mechanical friction losses are neglected. The mean power vs Π_2 (Figure **??** provides a detailed explanation for the variation of the output power when Π_2 is increased. The key regions consists of region 1 where the P_{mean} increases with Π_2, region 2 where P_{mean} becomes maximum and region 3 where P_{mean} decreases with Π_2. Time histories of P_t and P_d at each of these key regions are presented in figure 4.

Figure 2(a) shows that C_y and therefore instantaneous force rises until 4° where it peaks and then falls, and at around 6° becomes negative. The maximum instantaneous power that can be transferred occurs when $C_t\dot{y}$ is a maximum which occurs when θ is close to the peak in the C_y curve . At the region where the instantaneous force becomes negative it will be opposing the velocity $\dot{y}$. Data at $\Pi_1 = 10$, $m^* = 20$ and $Re = 200$ are shown in figure 4 and are analysed as an example.

At region 1 ($\Pi_2 = 0.3$) the damping is low in comparison with region 1 and 2. While this may lead to larger oscillations, damping is required to dissipate power according to equation 5. Therefore, the low damping in this region leads to a low mean power output. Fig.4 (a) shows that P_t becomes negative over some portion of the cycle. This is caused by the high velocity amplitude leading to the equivalent incident angle θ to exceed the range where C_y is positive (i.e. $0 < \theta < 6°$ as shown in figure3(a)). In this portion of the cycle the fluid-dynamic force actually opposes the direction of travel and power is transferred from the structure to the fluid during those times. From an energy perspective, the mechanical damping is not sufficient to remover the energy transferred from the fluid to the structure during other times of the cycle because Π_2 is substantially low. Therefore this excess

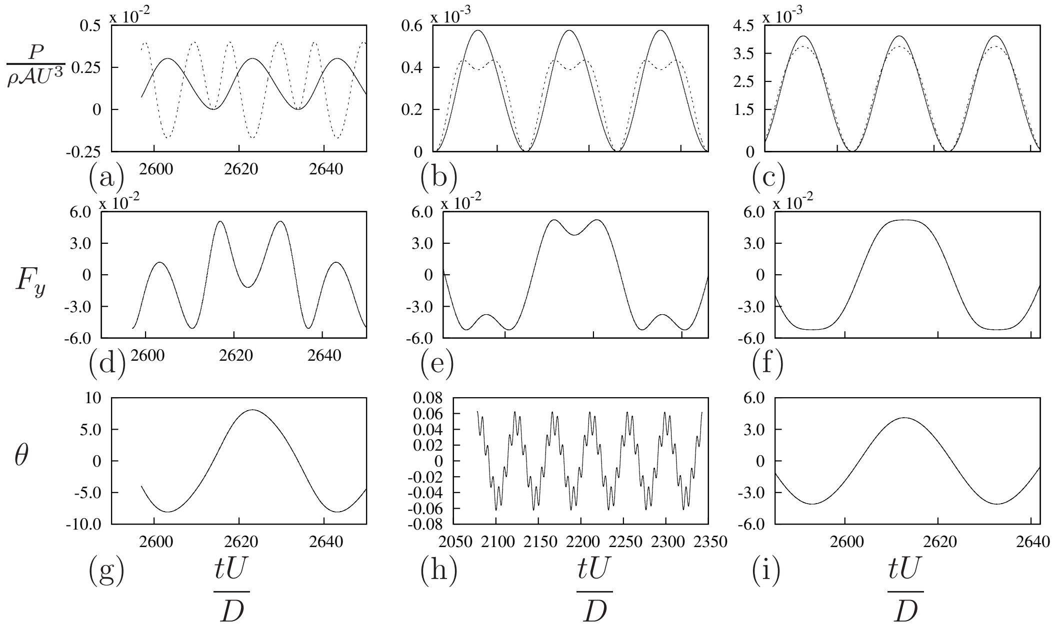

Figure 4: Time histories of P_t, P_d, F_y and θ at Π_2 = 0.15, 0.54 and 0.8. Data was obtained at $m^* = 20$, $\Pi_1 = 10$ and Re=200. The time histories of P_t (—) and P_d (- - -) are presented for: (a) Π_2 = 0.15; (b) Π_2 = 0.54; (c) Π_2 = 0.8. Time histories of the instantaneous force F_y for: (d) Π_2 = 0.15; (e Π_2 = 0.54; (f) Π_2 = 0.8. Time histories of the instantaneous angle θ for: (g) Π_2 = 0.15; (h) Π_2 = 0.55; (i) Π_2 = 0.8.

energy is transferred back to the fluid as depicted by the negative region of P_d in Fig.4(a).

At region 3 where $\Pi_2 = 0.8$ the damping constant is high and a clear sinusoidal signal is observed for both P_d and P_t in figure 4(c). Figures 4(f) and 4(i) show that equivalent incident angle θ (which for small values, is proportional to the transverse velocity of the body) is in phase with F_y. The velocity amplitude in this case is small and θ is within the range where the hydrodynamic force increases with the incident angle (i.e. $0 < \theta \leq 5°$ as shown in figure 2(a)). According to equation 6, these conditions are suitable for high power output. However in this case, the high damping limits the velocity amplitude and results in relatively low fluid dynamic forces.

At region 2 ($\Pi_2 = 0.54$), a balance is found between high and low values of damping. P_t is not a pure sinusoidal signal, however the signal remains periodic. From the time history graph of P_t, two 'peaks' are present in a single half cycle as shown if figure 4(b). In this case, the velocity amplitude actually exceeds the equivalent incident angle where the hydrodynamic forces peaks (i.e. $\theta = 5°$ in 3 (a)). The dips in P_d between the two peaks approximately correspond to the time where the transverse velocity is higher than 0.09 and F_y is decreasing with increasing transverse velocity. The mean power output is at its maximum. This is due to the fact that this region is the best compromise between region 1 and 3. The damping is high enough to obtain a high power output while not too high to allow the induced angle of attack to enter the region where the forcing opposes the direction of travel.

3.2. Influence of Π_1

From figure 5 it could be seen that the collapse of the mean power and velocity amplitude are excellent, regardless of the combination of U^* and m^* being used. Thus $\Pi_1 \geq 10$ is defined high Π_1 and the rest as low Π_1. As Π_1 reduces, at low Π_1(Fig:7), the power increases. However, figure 7 shows that the mean power does not change if Π_1 is kept constant and m^* is varied. The reason behind this is as $\Pi_1$reduces, the response of the system moves towards a square signal from a sinusoidal signal. This is due to the fact that in this region the forcing is dominated by the higher order terms in the forcing function (Eq:3). The formulation of Π_1 and Π_2 does not include the non-linear terms of Eq: 7. However, $m^*$is not eliminated in scaling the higher-order terms. It was mention earlier that the non-linear terms influences the low $\Pi_1$and therefore the influence of m^*at low $\Pi_1$was investigated. Figure 6

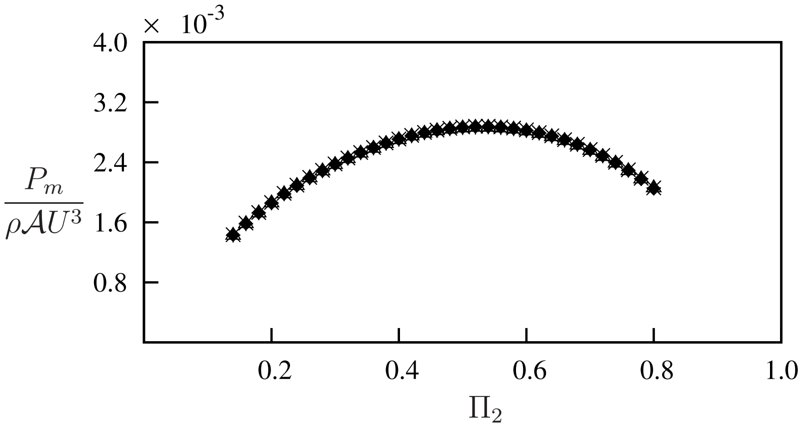

Figure 5: Mean power as a function of $\Pi_2$obtained using QSS assumption at high Π_1 levels. Data presented at four different combined mass-stiffness levels. $\Pi_1 = 10$ ($m^* = 20,\ U^* = 40$) (×), $\Pi_1 = 100$ ($m^* = 80,\ U^* = 50$) (+), $\Pi_1 = 500$ ($m^* = 220,\ U^* = 60$) (◆) and $\Pi_1 = 1000$ ($m^* = 400,\ U^* = 40$) (△).

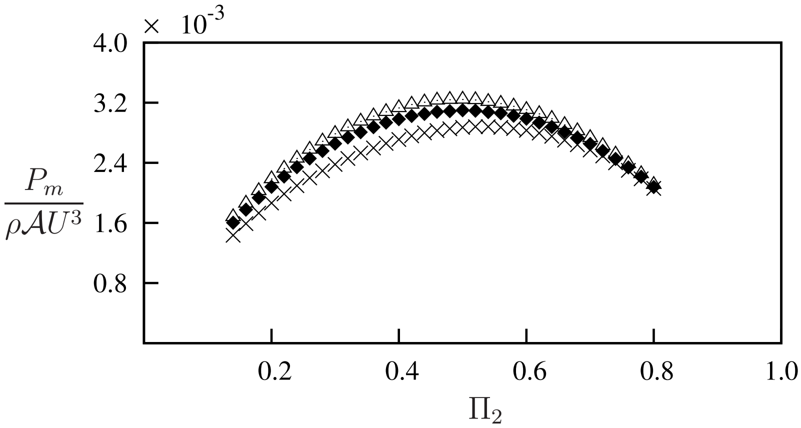

Figure 6: mean power as a function of $\Pi_2$obtained using QSS assumption at high and low $\Pi_1$mean power as a function of Π_2.. . Data presented at $\Pi_1 = 10$ (×), $\Pi_1 = 0.1$ (◆), and $\Pi_1 = 0.05$ (△).

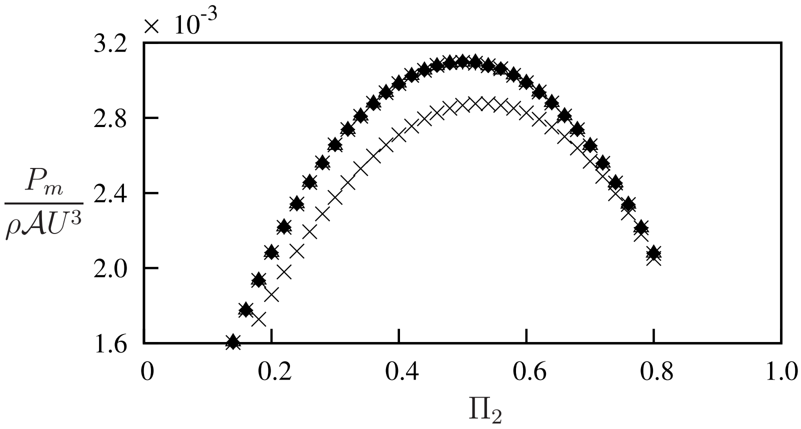

Figure 7: Mean power as a function of $\Pi_2$obtained using QSS assumption data at high and low Π_1. Data presented at $\Pi_1 = 100$ ($\times$) $m^* = 130$(+), $\Pi_1 = 0.1$ $m^* = 2$ (◆), $\Pi_1 = 0.1$ $m^* = 20$ (△) and $\Pi_1 = 0.1$ $m^* = 50$ ($*$). The mass ratio does not have an effect on $\Pi_1$even at low Π_1

shows that at the low mass $\Pi_1$region the mean power does not change for a given $\Pi_1$even the $m^*$is changed.

However, particular region (low Π_1) could not be captured in the DNS results as the vortex shedding is much stronger and overcomes the galloping signal indicating that the QSS hypothesis deviates from the actual behaviour of the system at low Π_1.

3.3. limitation of the quasi-steady hypothesis at low Reynolds numbers

The QSS hypothesis assumes that the only force driving the system is the instantaneous lift generated by the induced velocity. However, vortex shedding is also present in this system. Therefore, an essential assumption when this model is used is that the effect of vortex shedding is minimal. Hence, the model has been always used at high *Re* and at high mass ratios. The present study is focused on identifying the limiting parameters of the QSS model at low Reynolds numbers by providing a comparison with DNS results.

Joly et al. (2012) showed that the displacement data obtained using the QSS assumption and DNS agree well at low Reynolds numbers, with the modification implemented to the oscillator equation which accounts for the vortex shedding. These data were obtained at zero damping levels. However, the current study was focused on the power transfer of the system from the

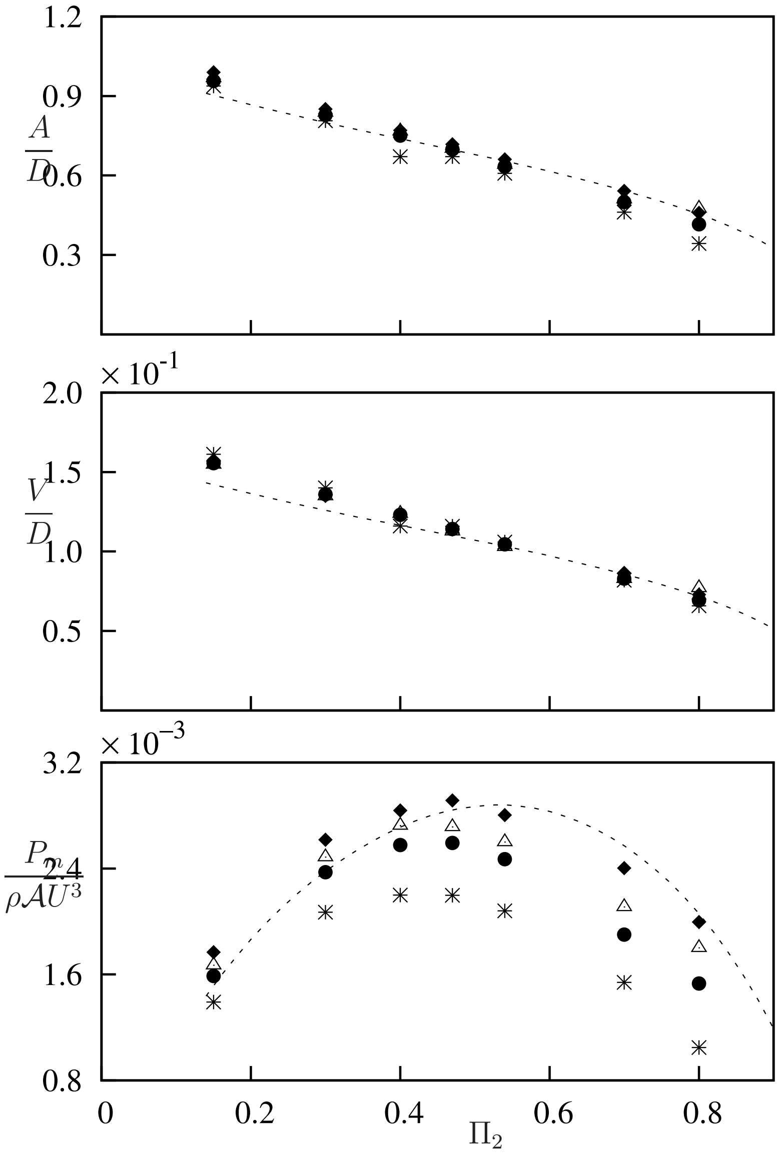

Figure 8: Comparison of data generated using the quasi-static theory and full DNS simulations . (a) Displacement amplitude, (b) velocity amplitude and (c) mean power as functions of Π_2. Data were obtained at Re = 200 at three different combined values $\Pi_1 = 10$ ($m^* = 20.13$) (✳), $\Pi_1 = 60$ ($m^* = 49.31$) (●), $\Pi_2 = 250$ ($m^* = 100.7$) (△) and $\Pi_1 = 1000$ ($m^* = 201.3$). The QSS data at $\Pi_1 = 10$ are represented by (- - -)

fluid to the body. Therefore analysing the behaviour of the system with increasing damping is of interest.

The comparison between QSS and the DNS results (Fig:8) revealed that the discrepancy of the power data increases significantly as Π_2 is increased for a given Π_1. However, it could also be observed that the discrepancy on power is reduced when the Π_1 is increased.

The reason behind this phenomenon could be explained by analysing the power spectrum of the velocity signal of the system. Figure 9 shows the power spectrum of the velocity signals at $\Pi_1 = 0.8$ and $\Pi_2 = 10, 60, 250$ and 1000. The data shows that the magnitude of the second peak at $\frac{fd}{U} = 0.156$ which represents the vortex shedding signal reduces as the mass ratio is increased. Hence, it could be concluded that the influence of vortex shedding is more prominent at low mass ratio therefore results in larger deviations from quasi-steady state results. This strengthens Joly et al. (2012) conclusions. However, the significant of this study with that of Joly et al. (2012) is that we have provided a comparison of QSS and DNS data as damping is increased.

4. Conclusion

In this paper the power transfer of a square body under fluid-elastic galloping is analysed by solving the quasi-steady state oscillator model equation using numerical integration. Data obtained were presented using the classical VIV parameters i.e. ζ and $U^*$and the new parameter (combined mass-damping) Π_2 which was obtained using the natural time scales of the system by linearising the QSS oscillator equation. The data presented using the new parameters showed a excellent collapse for power and velocity amplitude strengthening the argument that the power transfer is not dependent on the frequency the system.

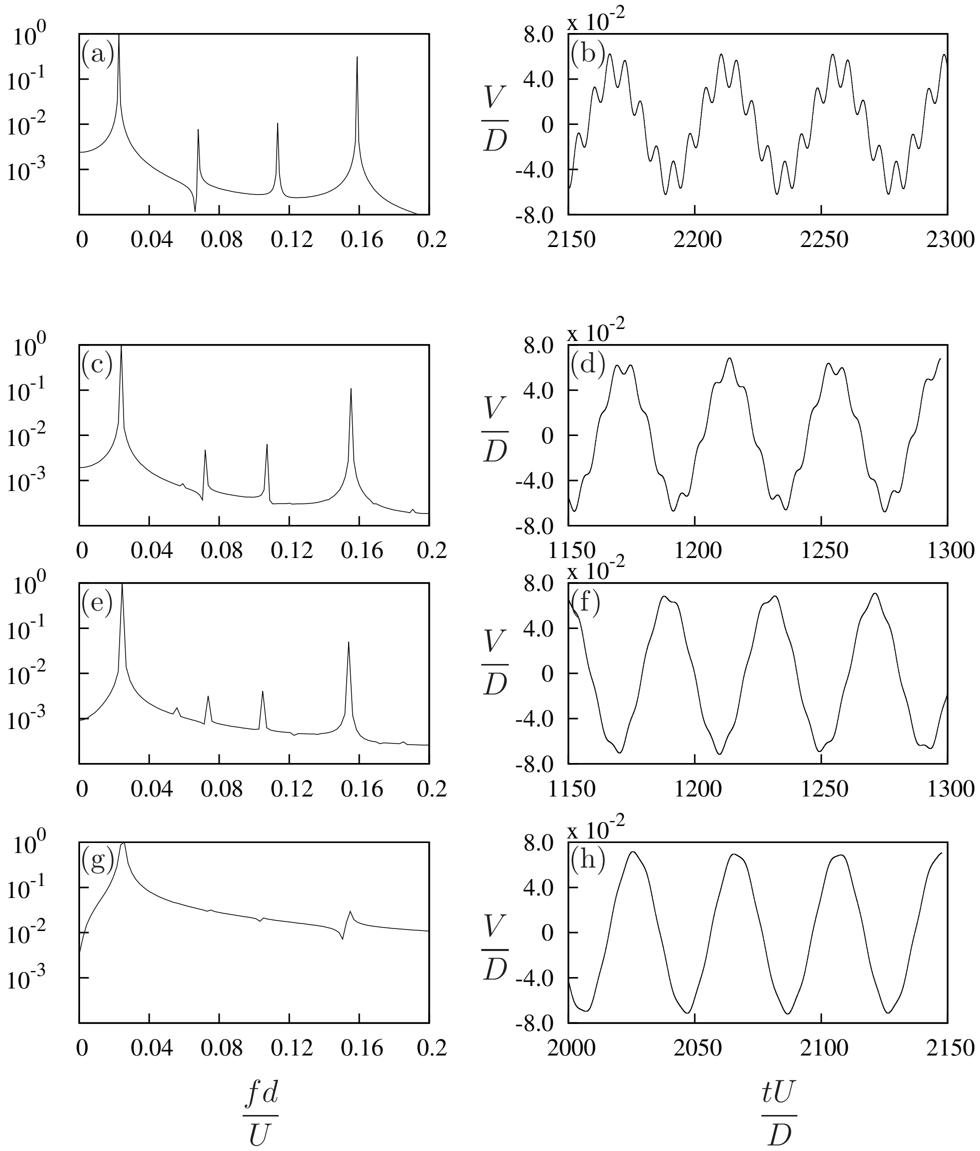

Figure 9: Velocity signal (right) and the corresponding power spectrum (left) of the DNS data at 3 different Π_1 at $\Pi_2 = 0.8$. (a) and (b) $\Pi_1 = 10$, (c) and (d) $\Pi_1 = 60$, (e) and (f) $\Pi_1 = 250$, (g) and (h) $\Pi_1 = 1000$. U^* is kept at 40 therefore the mass ratio increases as Π_1 increases. It is evident that the influence of vortex shedding reduces as the inertia of the system increases.

References

Barrero-Gil, A., Alonso, G., Sanz-Andres, A., Jul. 2010. Energy harvesting from transverse galloping. Journal of Sound and Vibration 329 (14), 2873–2883.

Barrero-Gil, A., Sanz-Andrés, A., Roura, M., Oct. 2009. Transverse galloping at low Reynolds numbers. Journal of Fluids and Structures 25 (7), 1236–1242.

Den Hartog, J. P., 1956. Mechanical Vibrations. Dover Books on Engineering. Dover Publications.

Glauert, H., 1919. The rotation of an aerofoil about a fixed axis. Tech. rep., Advisory Committee on Aeronautics R and M 595. HMSO, London.

Griffith, M. D., Leontini, J. S., Thompson, M. C., Hourigan, K., 2011. Vortex shedding and three-dimensional behaviour of flow past a cylinder confined in a channel. Journal of Fluids and Structures 27 (5-6), 855–860.

Joly, A., Etienne, S., Pelletier, D., Jan. 2012. Galloping of square cylinders in cross-flow at low Reynolds numbers. Journal of Fluids and Structures 28, 232–243.

Leontini, J. S., Lo Jacono, D., Thompson, M. C., Nov. 2011. A numerical study of an inline oscillating cylinder in a free stream. Journal of Fluid Mechanics 688, 551–568.

Leontini, J. S., Thompson, M. C., 2013. Vortex-induced vibrations of a diamond cross-section: Sensitivity to corner sharpness. Journal of Fluids and Structures 39, 371–390.

Leontini, J. S., Thompson, M. C., Hourigan, K., Apr. 2007. Three-dimensional transition in the wake of a transversely oscillating cylinder. Journal of Fluid Mechanics 577, 79.

Luo, S., Chew, Y., Ng, Y., Aug. 2003. Hysteresis phenomenon in the galloping oscillation of a square cylinder. Journal of Fluids and Structures 18 (1), 103–118.

Ng, Y., Luo, S., Chew, Y., Jan. 2005. On using high-order polynomial curve fits in the quasi-steady theory for square-cylinder galloping. Journal of Fluids and Structures 20 (1), 141–146.

Païdoussis, M., Price, S., de Langre, E., 2010. Fluid-Structure Interactions : Cross-Flow-Induced Instabilities. Cambridge University Press.

Parkinson, G. V., Smith, J. D., 1964. The square prism as an aeroelastic non-linear oscillator. The Quarterly Journal of Mechanics and Applied Mathematics 17 (2), 225–239.

Thompson, M., Hourigan, K., Sheridan, J., Feb. 1996. Three-dimensional instabilities in the wake of a circular cylinder. Experimental Thermal and Fluid Science 12 (2), 190–196.

Thompson, M. C., Hourigan, K., Cheung, A., Leweke, T., Nov. 2006. Hydrodynamics of a particle impact on a wall. Applied Mathematical Modelling 30 (11), 1356–1369.

Vio, G., Dimitriadis, G., Cooper, J., Oct. 2007. Bifurcation analysis and limit cycle oscillation amplitude prediction methods applied to the aeroelastic galloping problem. Journal of Fluids and Structures 23 (7), 983–1011.